Rev.Adv.Mater.Sci. 15(2007) 69-78

SIMULATIONS OF NANOCOMPOSITE CARBON FILMS

P.C. Kelires

Physics Department, University of Crete, P.O. Box 2208, 710 03, Heraclion, Crete, Greece
and Department of Mechanical Engineering & Materials Science and Engineering, Cyprus University of Technology, P.O. Box 50329, 3036 Limassol, Cyprus

Received: January 22, 2007

Abstract. The structure, stability, and mechanical properties of composite carbon films containing nanodiamonds and nanotubes are investigated by means of Monte Carlo and Tight-binding Molecular Dynamics simulations. The nanodiamonds are found to be stable in dense tetrahedral amorphous carbon matrices. The resulting composite materials have significantly enhanced elastic moduli compared to the pure amorphous phase, approaching the moduli of diamond. They are superhard, with a high ideal strength. The simulations also shed light into the fracture mechanisms of the material. It is found that fracture in the nanocomposites, under tensile or shear load, occurs inter-grain. For nanotube composites, it is shown that van der Waals forces play a vital role in shaping up the interfacial geometry, producing a curved graphitic wall surrounding the tubes, without covalent bonding between the tube and the matrix. The most stable structures are predicted to have intermediate densities, high anisotropies, and increased elastic moduli compared to pure amorphous carbon films.

1. INTRODUCTION

Nanostructured amorphous carbon (*na*-C) has attracted considerable attention in recent years for its properties, both mechanical and electronic, that will supplement and enhance those of the traditional, single-phase *a*-C. *Na*-C ran be described as a composite material in which carbon nanocrystallites, of various sizes and phases are embedded in *a*-C matrices. This novel hybrid form of carbon offers the unique possibility to intermingle the properties of carbon nanostructures [1] with those of pure *a*-C [2]. For example, since some of these nanostructures are proposed to be insulating, while others to be metallic, the possibility is opened for tailoring the electronic properties of *a*-C by controlling the type and size of the embedded structures. Or one anticipates to produce superhard carbon-based materials by appropriately choosing diamond-like nanoinclusions.

Na-C films can be composed by a variety of carbon nanostructures, ranging from diamond crystallites, to carbon nanotubes (CNT) and concentric-shell graphitic onions [1] bound by van der Waals (VDW) forces, to entirely three-dimensional sp^2 covalent conformations with no VDW bonding. The latter include porous, open graphene structures with negative curvature (schwarzites) [3-6]. Synthesis of *na*-C films ran be achieved by different methods such as arc plasma methods [7] leading to networks with bucky onions, or by supersonic cluster beam deposition (SCBD) techniques [8,9] producing schwarzites, or by electron and ion irradiation of *a*-C producing onions and/or nucleation of diamond cores [10-12].

From a fundamental point of view, it is vital to understand how the nanostructures interact with the embedding matrix, to unravel the structural elements at the interface, and to examine their influence on the properties of the material. In this re-

Corresponding author: P.C. Kelires, e-mail: kelires@physics.uoc.gr

view paper, I present work on *na*-C [13-15] which has been carried out during the last few years in the Simulational Physics / Materials Science Theory Group at Heraclion, aiming at an accurate investigation of the above issues.

Two representative cases are studied. In the first, we consider nanocomposite carbon materials consisting of diamond crystallites embedded in *a*-C matrix. We denote these materials by *n*-D/*a*-C. The synthesis and growth mechanisms of this phase have been explored by Lifshitz and co-workers, in both hydrogenated [11] and pure [12] dense *a*-C matrices. We examine its energetics and stability and find that nanodiamonds are only stable in tetrahedral amorphous carbon (*ta*-C), containing a high fraction of sp^3 hybrids. We then show that the nanocomposite is a superhard material, with enhanced elastic moduli compared to *ta*-C, and we examine its ideal strength and fracture mechanisms, asking in particular whether fracture in *n*-D/*a*-C occurs inter- or intra-grain.

In the second case, we consider nanocomposite materials consisting of carbon nanotubes (CNT) inside an *a*-C matrix. We denote these materials by CNT/*a*-C. This case differs fundamentally from the first one. The composite contains nanostructures which, in the absence of a matrix, are assembled by long-range VDW forces. Films containing nanotube fragments and fullerene-like inclusions have been produced, and reported to have high hardness and high elastic recovery [7]. The interesting factor in this case is how the matrix, a purely covalent material, bonds to the nanostructure.

Our simulations are able to shed light on this issue. We clearly identify the interfacial structure and infer the stability and hardness of the material. We find that, due to the VDW forces, a curved graphitic wall surrounding the tubes is produced, without covalent bonding between the matrix and the nanoinclusion. This opens the way for applications with enhanced electrical and thermal conductivity.

In the following, we first describe our theoretical methods and explain how we generate periodic cells with nanodiamonds and nanotubes embedded in *a*-C matrices. We then present our results for each case separately and discuss their implications with respect to the existing knowledge. Finally, we give our conclusions and prospects for future work.

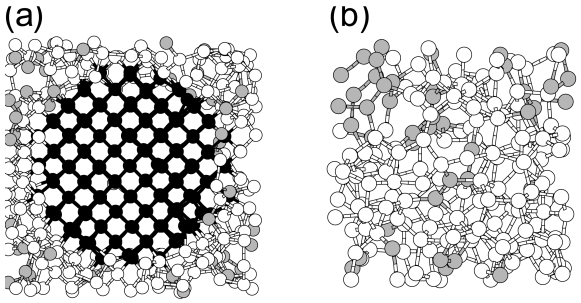

Fig. 1. Ball-and-stick models for (a) a *n*-D/*a*-C network, and (b) a pure *ta*-C structure. Grey (empty) spheres denote sp^2 (sp^3) sites. In (a), atoms belonging to the nanocrystal are represented by black spheres. (See also Ref. [15]).

2. METHODOLOGY

2.1. Tight-binding simulations

The tight-binding (TB) method is well suited for the present problem of bond breaking and fracture in nanocomposites. It provides a quantum mechanical description of the interactions, and thus is more accurate than empirical schemes. On the other hand, while less accurate than *ab initio* approaches, it yields greater statistical precision and allows the use of larger cells. We use the TB method developed at the Naval Research Laboratory (NRL) [16]. This is a non-orthogonal model, using distance- and environment-dependent parameters for transferability between different structures. The sp parameters for C were obtained by fitting to a first-principles database, which includes both the band structure and energies of the diamond, graphite, sc, bcc, and fcc configurations, as well as of the C_2 dimer. The fitting of the band structure provides additional robustness to the TB Hamiltonian. This is an important advantage of the present TB method, which enforces the transferability of these parameters to the amorphous state. The fitting was extended to large nearest-neighbor distances, up to 6.6 Å, so the approach properly describes the quantum mechanical effects of bond breaking and microfracture. The equilibrium bulk, shear, and Young's moduli and the density of diamond are calculated at 480 (443) GPa, 494 (476) GPa, 1300 (1145) GPa, and 3.65 (3.51) g cm^{-3}, respectively, compared to the experimental values given in parentheses. For a review of the NRL/TB scheme, see Ref. [17].

We use supercells of 512 atoms with periodic boundary conditions (PBC). The *n*-D/*a*-C structures contain a spherical nanocrystal in the middle, sur-

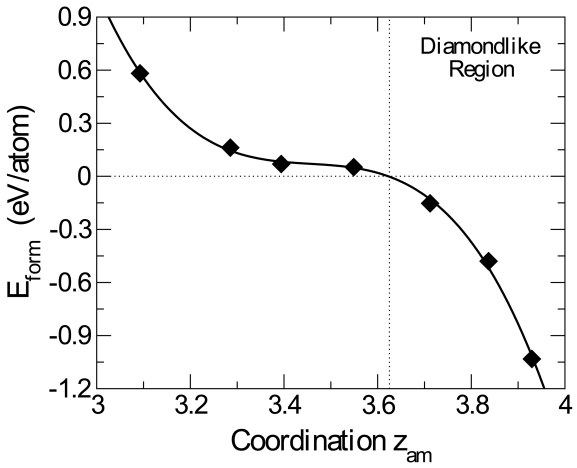

Fig. 2. Formation energies of nanodiamonds as a function of the coordination of the embedding amorphous matrix. Lines are fits to the points. (Data from Ref. [13]).

rounded by dense amorphous carbon. They were generated using Molecular Dynamics (MD) by melting and subsequent quenching at constant volume, in the canonical *(N, V, T)* ensemble, of a diamond structure, while keeping the atoms in the central spherical region frozen in their positions [13]. After quenching, producing amorphization of the surrounding matrix, the cells are fully relaxed with respect to atom positions and volume. The density and coordination of the matrix is controlled by the initial starting volume of the supercell. The pure *a*-C cells are also generated by quenching from the melt. In both cases, the liquid was prepared at 6000K, and typical quenching durations and rates used are 40 ps and 300 K/ps, respectively. In addition, we examine the properties of the Wooten-Winer-Waiie (WWW) model [18] of "amorphous diamond" (*a*-D), a hypothetical 100% sp^3-bonded model, which serve as a benchmark for the calculated properties of *a*-C and *n*-D/*a*-C networks. The WWW structure (512 atoms) is fully relaxed with the NRL/TBMD approach. All calculated properties are inferred at 0K.

2.2. Monte Carlo simulations

For the problem of stability and energetics of nanodiamond and nanotube composites, which does not involve bond breaking and fracture that would need an accurate quantum mechanical treatment, we use continuous-space Monte Carlo (MC) simulations within the empirical potential approach. We used the empirical potential of Tersoff [19], which is a short-range model and provides a fairly good description of the structure and energetics of a wide range of *a*-C phases [3,13,20,21]. In the special case of CNT/*a*-C, we need to take into account not only short-range covalent forces, which are sufficient for the description of the interactions within either the CNT's and the *a*-C matrix, but also the weaker long-range VDW forces, which are important for the interactions between the CNT's and the matrix, as will be shown below. This is done as follows.

For the intra-tubular and intra-matrix short-range interactions, we use the Tersoff potential. We confirmed that the potential reproduces the high elastic moduli of single-wall carbon nanotubes (SWCN's). For example, individual SWCN's with diameters of ~ 1 nm exhibit bulk moduli of ~ 200 GPa, in very good agreement with *ab initio* results [22].

For the interactions between the CNT's and the matrix, we use a simple Lennard-Jones potential [23], which was shown to successfully describe the bulk properties of solid C_{60} [23] and multiple-shell carbon fullerenes [24]. We limit the attractive interactions between atoms of the nanotube and atoms in the matrix within a cutoff distance of 0.8 nm. Interactions beyond this distance contribute negligibly to the energy.

The *n*-D/*a*-C networks containing 4096 atoms in a cubic cell with PBC are generated using the same procedure as in the TBMD case. For CNT/*a*-C, we use a similar procedure: The initial structure to start with is a cubic diamond crystal with an empty cylindrical core of a predetermined diameter, formed by artificially removing the atoms within this volume, into which the chosen CNT is inserted. The amorphous matrix is then generated by melting and subsequent quenching of the surrounding diamond atoms, while keeping the atoms of the CNT frozen in their ideal positions. Finally, full relaxation of the whole structure takes place, both in the atomic positions and the volume (density) of the cell. Properties are calculated by MC ensemble averaging at 300K.

Matrices of various densities (mean coordination) are formed by appropriately choosing the size of the initial cell. The CNT's have open ends and extend through the entire length of the cube. Because PBC are applied to the cells, this corresponds to CNT's of infinite length. The size of the cells ranges from about 1.5 to 4.0 nm. Nanotubes of various chiralities were embedded, with diameters ranging from about 0.8 to 2.8 nm. Due to the

PBC, this corresponds to a dense array of CNT's packed in parallel. Although this probably is an idealized model of a CNT nanocomposite, it provides the essential features of the CNT-matrix interaction. The system resembles CNT bundles, but with *a*-C material in between the tubes.

3. RESULTS AND DISCUSSION

3.1. Diamond nanocomposites

3.1.1. Structure

We begin with the structural characteristics of the TBMD-generated structures. Two of them, at equilibrium, are shown in Fig. 1. Panel (a) portrays a typical nanocomposite network. Due to the PBC, this corresponds to a special case, where we have a homogeneous dispersion of crystallites of equal size in the matrix, at regularly ordered positions. The diamond nanocrystal has a diameter of 12.5 Å and its volume fraction is 31%. The density of the matrix ρ_{am} is 3 g cm^{-3}, and its mean coordination $\bar{z}_{am}$ is 3.8. It is interesting to note that there is a remarkable tendency of sp^3 atoms in the matrix to gather and enrich the interface region around the nanodiamond. A careful inspection of the local structure reveals an increasing degree of crystallinity, indicating that such tetrahedral atoms may act as possible nucleation centers for expanding the size of the diamond nanocrystal under the appropriate conditions.

Panel (b) shows, for comparison, an equivalent single-phase, highly tetrahedral amorphous carbon (*ta*-C) network with the same sp^3 content and density. The sp^2 sites are largely clustered. The network contains a considerable fraction of both three- and four-membered (3-*m* and 4-*m*) rings, as computed using the shortest-path criterion of Franzblau [25]. Specifically, there are 20 3-*m* and 38 4-*m* rings. The vast majority of sites involved in such small rings are sp^3, ~ 95%. The average bond length in 3-*m* (4-*m*) rings is 1.50 (1.55) Å. These characteristics regarding clustering and ring structure are in excellent agreement with what state-of-the-art *ab initio* MD simulations predict [26]. For example, in a network of a similar density with 125 atoms, three 3-*m* and eleven 4-*m* rings, composed of sp^3 atoms, with average bond lengths of 1.5-1.6 Å were found. This comparison shows that the present TB method treats accurately the strain energy of sp^3 sites in small rings. Also, the density-coordination (sp^3 fraction) relation for the *a*-C networks is found to be linear, in agreement with experiment and recent TBMD simulations using a different TB Hamiltonian [27].

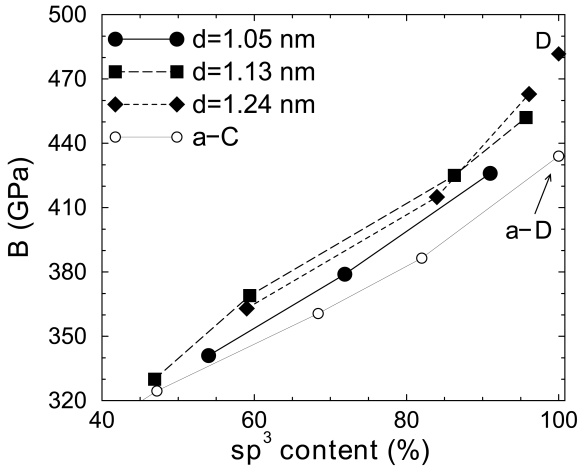

Fig. 3. Bulk modulus as a function of the sp^3 content for *a*-C and *n*-D/*a*-C, with nanodiamonds of different diameter *d*. Calculations for bulk diamond (D) and *a*-D are also shown, for comparison. (Data from Ref. [15]).

3.1.2. Stability

We examine the stability issue by defining the *formation energy* of a nanocrystal E_{form}, which takes into account the interaction of the embedded configuration with the host matrix.

E_{form} is given by

$$E_{form} = E_{total} - N_a E_a - N_c E_c, \quad (1)$$

where E_{total} is the total cohesive energy of the composite system (amorphous matrix plus nanocrystal), calculated directly from the simulation. E_c is the cohesive energy per atom of the respective crystalline phase, N_c is the number of atoms in the nanocrystal, N_a is the number of atoms in the amorphous matrix, and E_a is the cohesive energy per atom of the pure, undistorted amorphous phase (without the nanocrystal) with coordination z_{am}. Details how to compute E_a for an arbitrary z_{am} are given in Ref. [13]. A negative value of E_{form} denotes stability of the nanostructure, a positive value indicates metastability.

We have generated a series of cells with different z_{am} of the amorphous matrix, but keeping the size of the nanocrystal constant. Then, application of the above methodology yielded E_{form} as a function of z_{am}. The energy curve resulting from this analysis is shown in Fig. 2. The remarkable finding

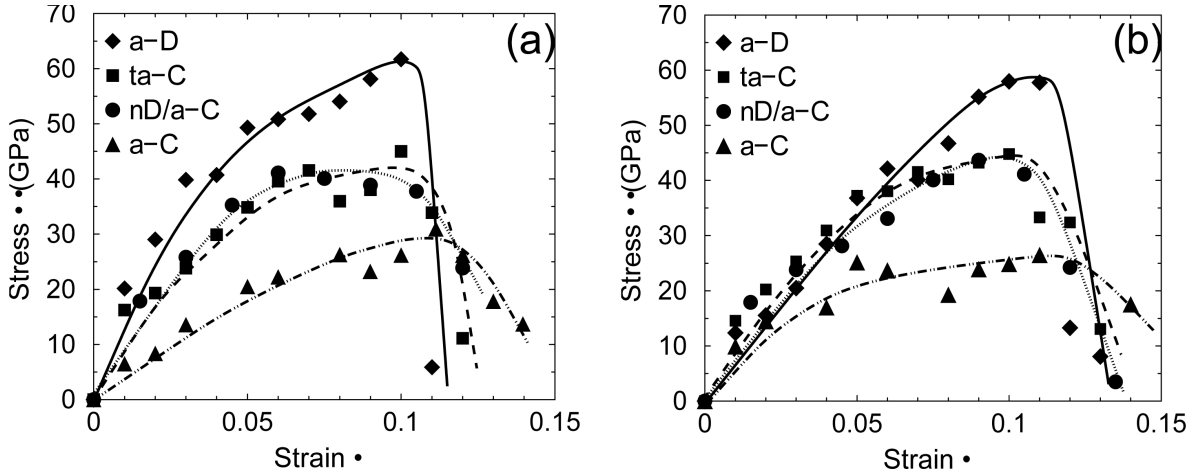

Fig. 4. Stress versus strain curves for various structures. The *ta*-C and *n*-D/*a*-C contain 80% sp^3 sites in the amorphous matrix; the *a*-C cell contains 50% sp^3 sites. Lines are fits to the data points. (a) Tensile load in the (111) direction, (b) Shear load on the [111] plane in the (112) direction. (Data from Ref. [15]).

is that nanodiamonds are unstable, or rather metastable, at low z_{am}, corresponding to low-density matrices, but they become more stable as z_{am} increases, reaching a high degree of stability in *ta*-C matrices.

This transition of nanodiamonds from metastability to stability at $z_{am} \approx 3.6$ provides us with a quantitative definition of *ta*-C, vaguely referred to as the form of *a*-C with a high fraction of sp^3 bonding. We define *ta-C* as the form of *a-C* with a fraction of sp^3 sites above ~60%, *in which diamond crystallites are stable.* Another way to check that the nanodiamonds are stable in this regime, besides referring to E_{form}, is to subject them to thermal annealing. A stable structure should be sustained in the matrix, while a metastable structure should shrink in favor of the host. Indeed, we find that this is the case [13]. Already before annealing, the metastable nanocrystals are heavily deformed in the outer regions near the interface with the amorphous matrix. The stable ones are only slightly deformed. Upon annealing, the former structures extensively shrink, and only a small core remains intact, while the stable structures retain their tetrahedral geometry.

3.1.3. Elastic modulus

A central question, of both fundamental and practical interest, is whether the elastic moduli of the *n*-D/*a*-C nanocomposites are enhanced over those of the equivalent pure *ta-C* phase. Previous studies have shown [20,27] that the elastic moduli of not only *ta-C* but also of "amorphous diamond" are lower than diamond's. This indicates that continuous random networks are softer than the equivalent crystal, despite containing the same bonds. The interest here is whether the existence of nanoinclusions improves significantly the elastic response of the matrix.

To answer this question, we calculated [15], as a representative quantity, the bulk modulus *B* of various *n*-D/*a*-C structures as a function of the sp^3 fraction in the cells, by fitting the energy versus volume curves with the Murnaghan equation of state. Fig. 3 shows the variation of *B* for both *n*-D/*a*-C and single-phase *a*-C. The values for diamond and *a*-D are shown for comparison. The moduli of *ta-C* networks (sp^3 fraction ≥ 60% [13]) are quite high, and that of *a*-D reaches ~ 90% of the diamond value, confirming the previous calculations [20,27]. Remarkably, the moduli of *n*-D/*a*-C networks are considerably higher than those of *a*-C. A mean increase over 10% is evident. The enhancement becomes stronger as the sp^3 fraction, or the density, increases. A similar effect is seen as the size, or volume fraction, of the nanocrystals increases. Impressively, beyond a certain point, *B*'s are shown to exceed the *a*-D value and approach that of diamond. We conclude that the elastic response of the composite structures to hydrostatic deformation is controlled by the nanoinclusions. These predictions might be useful for the optimization of nanocomposites with respect to size, density of nanoinclusions, and sp^3 content in the matrix.

3.1.4. Strength and fracture

Despite the importance of both *ta-C*, widely used in applications as a hard coating, and of the equivalent nanocomposite *n*-D/*a*-C, their deformation properties beyond the elastic regime are poorly understood. We recently investigated in detail these properties, including strength and hardness, and elucidated the atomistic picture behind the fracture mechanisms [15] using TBMD simulations. We summarize here the most important findings of this study.

We first discuss the ideal strength [28,29] of the materials under study. This is the maximum stress that a material can sustain under non-hydrostatic loads before becoming unstable and yielding to plastic deformation or fracture. For diamond, the present TB method gives the following strengths: 209 (225) GPa for the <100> direction, 130 (130) for the <110>, and 124 (95) GPa for the <111> direction, in the case of tensile load. In the case of shearing, the strength is 130 (93) GPa for the {111}<112> slip system. These results are in good agreement with the *ab initio* results of Telling *et al.* [30], given in parentheses, and confirm that the {111} plane is the easy-slip plane in diamond. The corresponding tensile strain at the maximum strength is 0.28, 0.21, and 0.15 for <100>, <110>, and <111>, respectively. The critical shear strain is 0.23.

To calculate the ideal strength of amorphous and nanocomposite structures, we apply tensile load in the <111> direction and shear load on the {111} plane in the <112> direction. The crystallographic directions are those of the nanodiamond region. The *a*-C phases are highly isotropic, therefore all directions of tensile or shear load are equivalent. The structures were strained in a series of incremental strains. At each step, atomic positions were fully relaxed with TBMD. The stress was extracted by differentiating the energy with respect to strain. The resulting stress-strain data points and fitted curves, for both tensile and shear load, are shown in Fig. 4.

We find that all structures have significantly lower ideal strengths and critical strains than diamond, including the *a*-D model which is 100% sp^3-bonded and has no planes of cleavage. This is due to the weaker character of the C-C bond in the amorphous network. Note that while the modulus of *a*-D reaches 90% that of diamond, its strength is only about half. This indicates softer angular forces, due to dihedral disorder, which render the sp^3 hybrids more easily unstable under non-hydrostatic stresses at the bond-breaking regime, far from equilibrium. On the other hand, radial rigidity near equilibrium is not so weakened, giving rise to high elastic moduli.

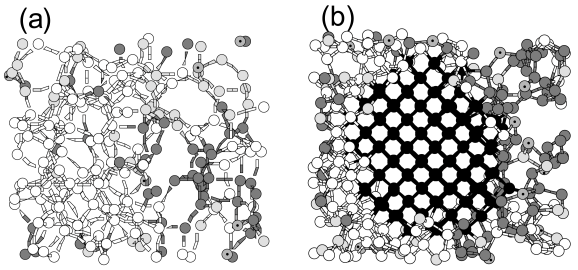

Fig. 5. Ball-and-stick models for fracture in (a) single-phase *ta*-C and (b) nanocomposite *n*-D/*a*-C, of similar densities. Light gray and empty spheres denote sp^2 and sp^3 sites with no broken bonds, respectively. Dark spheres show atoms of the nanodiamond. Dotted spheres and darker gray spheres denote broken sp^2 and sp^3 sites, which lost at least one bond, respectively. (Data from Ref. [I5]).

The most striking finding is that the ideal strength of *n*-D/*a*-C is about equal to that of *ta*-C, when having equivalent amorphous networks, for both tensile and shear loads. It indicates that the nanoinclusions do not actually contribute to the increase in strength, but that this is rather controlled by the other part of the composite structure, the amorphous matrix. We demonstrate this effect by examining the fracture mechanisms in our networks. For this purpose, we analyzed the microstructure just after the critical strain when bonds start to break. We consider a bond as being broken when its length has become longer than the first minimum in the pair distribution function of the network at equilibrium [31]. The so extracted cutoff distances are 1.90 Å, for the amorphous networks, and 1.75 Å for the nanodiamond crystallite.

Fig. 5 shows ball and stick models of *ta*-C and nanocomposite carbon under critical tensile strain. Atoms that have lost at least one bond are distinguished, according to their hybridization, from atoms with no broken bonds. It is clear that bond breaking in the nanocomposite takes place in the amorphous matrix and not in the nanodiamond, i.e., fracture occurs inter-grain and not intra-grain. This picture explains why the ideal strengths and corresponding strains of *n*-D/*a*-C and *ta*-C are about equal. The fracture mechanisms in both materials are similar.

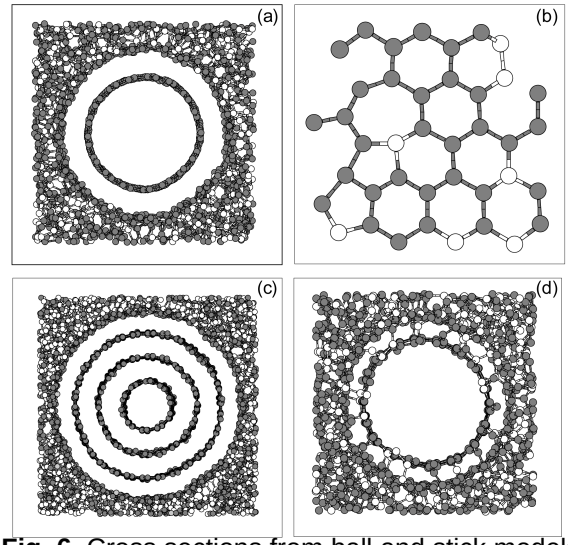

Fig. 6. Cross sections from ball and stick models of carbon nanotube composite structures. (a) An embedded SWCN. (b) Part of the curved graphitic wall surrounding the SWCN. (c) An embedded MWCN. (d) A structure formed without VDW interactions. Filled (open) spheres denote sp^2 (sp^3) atoms. (See also Ref. [14]).

Interestingly, the vast majority of atoms involving broken bonds are sp^3 hybrids, in both the *n*-D/*a*-C and *ta*-C materials. This can be understood on the basis of the relative energetics of sp^3 and sp^2 hybrids in the amorphous phase. It has been previously shown [32] that the average atomic energies of sp^3 and sp^2 sites in *ta*-C are -6.8 and -7.1 eV, respectively, with respect to atomic C. This is a huge energy difference between the two hybrid states compared to the almost degenerate energies in diamond and graphite (~ -7.4 eV). Therefore, in the presence of critical strain at the onset of fracture, when bonds have to break, it will be energetically favorable to loose bonds belonging to sp^3 atoms in the amorphous region. It is clear from Fig. 4 that microfracture originates in sp^3-rich clusters.

The hardness *H* of the various networks can be estimated by extracting the yield stress *Y* (defined as the stress where the strain departs 0.2% from linearity) and the Young's moduli *E* from the stress-strain curves of Fig. 5, and by using the empirical relation of Tabor [33], $H/Y = 0.07 + 0.6\ln(E/Y)$. We found ~ 90 GPa for *a*-D (WWW), ~70 GPa for *ta*-C and *n*-D/*a*-C, and ~40 GPa for 50%-50% *a*-C, compared to 120 GPa for diamond with the present TB method. The value for *ta*-C is in agreement with the experimentally reported values [34,35]. The nanocomposites offer a clear advantage over *ta*-C, namely their superior elastic properties. We expect nanocomposite carbon materials to be very useful for MEMS/NEMS devices.

3.2. Nanotube nanocomposites

We now turn to the second nanocomposite system of interest. CNT/*a*-C, consisting of carbon nanotubes (CNT) inside an *a*-C matrix.

3.2.1. Structure and stability

Representative nanocomposite structures formed in the way described in Section II, are portrayed in Fig. 6. Panel (a) shows a cross section of a (7 X 10) SWCN, having a diameter of 1.2 nm, embedded in a matrix with mean coordination $\bar{z}$ = 3.24 (density = 2.29 g cm^{-3}). The remarkable feature in the structure is that the atoms of the surrounding matrix reconstruct in such a way as to form an outer wall concentric to the nanotube. A double-wall nanotube is effectively formed. The outer wall is a curved graphitic sheet, but with some degree of disorder, as a close inspection of its structure reveals. Part of this sheet is depicted in panel (b). A ring statistics analysis shows that the sheet mainly consists of six-fold rings, their fraction being considerably higher than the corresponding fraction in the rest of the matrix. However, odd-membered rings do exist, necessitated by the presence of some sp^3 atoms in the wall, which serve as bridges with the rest of the matrix.

The optimum distance between the outer wall and the CNT is close to the graphite interplanar one (0.34 nm). This distance is independent of the tube diameter. A similar pattern is also observed in structures with embedded multi-wall carbon nanotubes (MWCN's), as shown in Fig. 6c. The interaction of the MWCN with the matrix forms again a graphitic sheet. The outer interplanar distance is the same with the inner interwall separations in the MWCN. The phenomenon is independent of the number of sheets in the MWCN.

In all cases the interaction of the matrix graphitic shell with the CNT's does not involve any covalent bonding. In order to unravel the contributions of short- and long-range forces to the formation of this wall, we generated structures by only using the short-ranged Tersoff potential for the interactions through out the system, thus "turning off" the VDW interactions. One of these structures is shown in Fig. 6d. Again, an outer wall is being

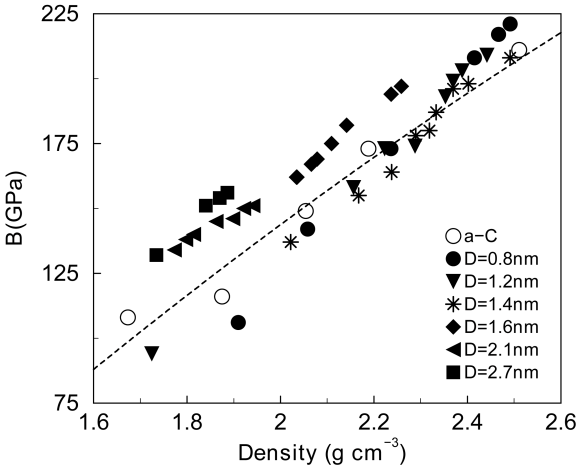

Fig. 7. Bulk moduli of SWCN's of various diameters versus nanocomposite density. Dashed line is a fit to *a*-C values. (Data from Ref. [14]).

formed, but it is defective. Many covalent bridge bonds are generated between the matrix wall and the SWCN, and so the interwall distance necessarily approaches the value of ~0.15 nm, much smaller than the interplanar distance in graphite or in MWCN's, and close to the covalent bond length.

This indicates that the repulsive forces of the potential tend to drive the matrix and CNT atoms apart, but its attractive forces impose these artificial bridge bonds, which necessitate the transformation of ideal sp^2 sites on the nanotube surface into distorted sp^3 sites, as shown in the plot. We conclude that short-range attractive forces are not involved in the matrix-CNT interaction, and that the VDW forces, although weak, are driving the perfect reconstruction of the matrix atoms while keeping intact the ideal CNT geometry.

The remarkable reconstruction of the amorphous matrix around the nanotube may not only have fundamental but also practical interest. We propose that these novel structures may be used in applications for enhanced electrical and thermal conductivity. The lack of covalent bonding between the nanotube and the matrix will prevent any conductivity losses to the matrix in the transverse directions, while directing it along the tube axis. A necessary prerequisite for any successful applications is, of course, the growth of nanocomposites with well-ordered embedded tubes.

The stability of the composite systems was inferred by calculating their formation energy [13], defined as the energy of the whole structure compared to the sum of the energies of its constituents (the *a*-C matrix and the nanostructure). We found that tubes are more stable in matrices of $\bar{z} \approx 3.2$-3.3, corresponding to densities of about 2.3 - 2.4 g·cm^{-3}. The denser (or diluted) the matrix, the less stable the system becomes. This information may be used to guide experimental work to fabricate the material.

3.2.2. Elastic moduli

We also examined the elastic properties of this nanocomposite system. A representative quantity is the bulk modulus *B*. We calculated *B* for several structures containing CNT's of various diameters. Fig. 7 shows the calculated moduli plotted as a function of the nanocomposite density. As a comparison, calculated moduli of single-phase *a*-C films are also shown. We observe a systematic increase of the nanocomposite *B* with respect to *a*-C, when it contains tubes of larger diameter, while smaller tubes induce increase only when embedded in dense matrices.

These nanocomposites have a high elastic anisotropy. We show this by calculating the components of the Young's modulus in the direction of the tube (axial) Y_{axial} and in the transverse directions Y_{trans}. We find that in all cases the anisotropy, defined by the ratio $A = Y_{trans}/Y_{axial}$, approaches that for the isolated SWCN. For example, a SWCN with a diameter of 0.8 nm has Y_{axial} = 1100 GPa and Y_{trans} = 620 GPa, yielding A = 0.56, while the nanocomposite with this tube and a matrix of density 2.6 g·cm^{-3} has Y_{axial} = 570 GPa, Y_{trans} = 380 GPa, and A = 0.67. The anisotropy increases with increasing tube diameter (tube volume fraction), because the tube contribution overwhelms the isotropic matrix part.

Note that higher moduli are achieved by having the tubes in a "bundle" arrangement without the need to interlink them [7]. In addition, the CNT composite material exhibits much higher bulk moduli than nanotube bundles *(*~ 40 GPa) [22], and is expected to also have high elastic recovery. These superior properties make it suitable for many practical mechanical applications, besides the electrical and thermal ones mentioned above.

4. CONCLUSIONS

Nanocomposite carbon materials composed of nanodiamond particles and nanotube fragments embedded in *a*-C matrices nave been investigated and shown to exhibit remarkable properties. Dia-

mond nanocomposites are superhard, with enhanced elastic moduli compared to the dense *ta*-C phase. Their ideal strength and the fracture mechanisms have been identified. The successful fabrication of such composite materials will require an optimization of nanoparticle size and density, along with a judicious choice of the embedding matrix, such as to enhance their stability and eliminate the intrinsic stress. Nanotube composites are shown to possess a remarkable interfacial structure, characterized by a graphitic reconstruction of the matrix around the nanotube, which is stabilized by VDW forces. Promising mechanical, electrical, and thermal applications are foreseen, based on this unique configuration. Further work is required to establish quantitatively these predictions.

ACKNOWLEDGEMENTS

The author is grateful to Maria Fyta and Ioannis Remediakis who contributed greatly to the work presented here through its various stages. The work was supported by a grant from the EU and the Ministry of National Education and Religious Affairs of Greece through the action "EPEAEK" (programme "ΠΥΘΑΓΟΡΑΣ").

REFERENCES

[1] For reviews of novel carbon nanostructures, see S. Subramoney // *Adv. Mater.* **10** (1998) 1157; F. Bannart // *Rep. Prog. Phys.* **62** (1999) 1182.

[2] For reviews of amorphous carbon, see D.R. McKenzie // *Rep. Prog. Phys.* **59** (1996) 1611; J. Robertson // *Mater. Sci. Eng. R* **37** (2002) 129; S.R.P. Silva, In: *Handbook of Thin Film Materials*, *Vol. 4,* ed. by H.S. Nalwa (Academic Press, New York, 2002), p. 403.

[3] D. Vanderbilt and J. Tersoff // *Phys. Rev. Lett.* **68** (1992) 511.

[4] T. Lenosky, X. Gonze, M. Teter and V. Elser // *Nature (London)* **355** (1992) 333.

[5] M. Keeffe, G.B. Adams and O.F. Sankey // *Phys. Rev. Lett.* **68** (1992) 2325.

[6] B. Winkler, C.J. Pickard, V. Milman, W.E. Klee and G. Thimm // *Chem. Phys. Lett*. **312** (1999) 536.

[7] G.A.J. Amaratunga, M. Chhowalla, C.J. Kiely, I. Alexandrou, R. Aharonov and R.M. Devenish // *Nature (London)* **383** (1996) 321.

[8] P. Milani, M. Ferretti, P. Piseri, C.E. Bottani, A. Ferrari, A. Li Bassi, G. Guizzetti and M. Patrini // *J. Appl. Phys.* **82** (1997) 5793.

[9] D. Donadio, L. Colombo, P. Milani and G. Benedek // *Phys. Rev. Lett.* **83** (1999) 776.

[10] F. Banhart and P.M. Ajayan // *Nature (London)* **382** (1996) 433; M. Zaiser and F. Banhart // *Phys. Rev. Lett.* **79** (1997) 3680.

[11] Y. Lifshitz, T. Kohler, T. Frauenlieim, I. Guzmann, A. Hoffman, R.Q. Zhang, X.T. Zhou and S.T. Lee // *Science* **297** (2002) 1531.

[12] Y. Yao, M.Y. Liao, T. Kohler, T. Frauenheim, R.Q. Zhang, Z.G. Wang, Y. Lifshitz and S.T. Lee // *Phys. Rev. B* **72** (2005) 035402.

[13] M.G. Fyta, I.N. Remediakis and P.C. Kelires // *Phys. Rev. B* **67** (2003) 035423; M.G. Fyta, C. Mathioudakis, G. Kopidakis and P.C. Kelires // *Thin Solid Films* **482** (2005) 56.

[14] M.G. Fyta and P.C. Kelires // *Appl. Phys. Lett.* **86** (2005) 191916.

[15] M.G. Fyta, I.N. Remediakis, P.C. Kelires and D. Papaconstantopoulos // *Phys. Rev. Lett.* **96** (2006) 185503.

[16] R.E. Cohen, M.J. Mehl and D.A. Papaconstantopoulos // *Phys. Rev. B* **50** (1994) 14694; M.J. Mehl and D.A. Papaconstantopoulos // *Phys. Rev. B*. **54** (1996) 4519; D.A. Papaconstantopoulos, M.J. Mehl, S.C. Erwin and M.R. Pederson // *Mater. Res. Soc. Symp.* **491** (1998) 221.

[17] D.A. Papaconstantopoulos and M.J. Mehl // *J. Phys: Cond. Mat.* **15** (2003) R413.

[18] F. Wooten, K. Winer and D. Weaire // *Phys. Rev. Lett*. **54** (1985) 1392; B.R. Djordjevic, M.F. Thorpe and F. Wooten // *Phys. Rev. B* **52** (1995) 5685.

[19] J. Tersoff // *Phys. Rev. Lett*. **61** (1988) 2879.

[20] P.C. Kelires // *Phys. Rev. Lett.* **73** (1994) 2460.

[21] P.C. Kelires // *Phys. Rev. B* **62** (2000) 15686.

[22] S. Reich, C. Thomsen and P. Ordejon // *Phys. Rev. B* **65** (2002) 153407.

[23] J. P. Lu, X.-P. Li and R. M. Martin // *Phys. Rev. Lett.* **68** (1992) 1551.

[24] J. P. Lu and W. Yang // *Phys. Rev. B* **49** (1994) 11421.

[25] D.S. Franzblau // *Phys. Rev. B* **44** (1991) 4925.

[26] N.A. Marks, D.R. McKenzie, B.A. Pailthorpe, M. Bernasconi and M. Parrinello // *Phys. Rev. Lett.* **76** (1996) 768; D.G. McCulloch, D.R. McKenzie and C.M. Goringe // *Phys. Rev. B* **61** (2000) 2349; N.A. Marks, N.C.

Cooper, D.R. McKenzie, D.G. McCulloch, P. Bath and S.P. Russo // *Phys. Rev. B* **65** (2002) 075411.
[27] C. Mathioudakis, G. Kopidakis, P.C. Kelires, C.Z. Wang and K.M. Ho // *Phys. Rev. B* **70** (2004) 125202.
[28] Y. Zhang, H. Sun and C. Chen // *Phys. Rev. Lett.* **93** (2004) 195504; *ibid.* **94** (2005) 145505.
[29] X. Blase, P. Gillet, A. San Miguel and P. Melinon // *Phys. Rev. Lett.* **92** (2004) 215505.
[30] R.H. Telling, C.J. Pickard, M.C. Payne and J.E. Field // *Phys. Rev. Lett.* **84** (2000) 5160.
[31] G. Galli, F. Gygi and A. Catellani // *Phys. Rev. Lett.* **82** (1999) 3476.
[32] P.C. Kelires // *Phys. Rev. Lett.* **68** (1992) 1854; *Phys. Rev. B* **47** (1993) 1829.
[33] D. Tabor // *Rev. Phys. Technol.* **1** (1970) 145.
[34] G.M. Pharr, D.L. Callahan, S.D. McAdams, T.Y. Tsui, S. Anders, A. Anders, J.W. Ager III, I.G. Brown, C.S. Bhatia, S. R. P. Silva and J. Robertson // *Appl. Phys. Lett.* **68** (1996) 779; X. Shi, D. Flynn, B.K. Tay, S. Prawer, K.W. Nugent, S.R.P. Silva, Y. Lifshitz and W.I. Milne // *Philos. Mag. B* **76** (1997) 351; E. Martinez, J.L. Andujar, M.C. Polo, J. Estevez, J. Robertson and W.I. Milne // *Diamond Rel. Mater.* **10** (2001) 145.
[35] T.A. Friedmann, K.F. McCarty, J.C. Barbour, M.P. Siegal and D.C. Dibble // *Appl. Phys. Lett.* **68** (1996) 1643.